Multiplexed sensing of magnetic field and temperature in real time using a nitrogen-vacancy ensemble in diamond – supplemental material

Jeong Hyun Shim[1,2], Seong-Joo Lee[1], Santosh Ghimire[1], Ju Il Hwang[3], Kwang-Geol Lee[3], Kiwoong Kim[4], Matthew J. Turner[5,6,7], Connor A. Hart[5,6,7], Ronald L. Walsworth[5,6.7], and Sangwon Oh[1]

[1]*Quantum Magnetic Imaging Team, Korea Research Institute of Standards and Science, Daejeon 34113, South Korea*

[2]*Department of Medical Physics, University of Science and Technology, Daejeon 34113, South Korea*

[3]*Department of Physics, Hanyang University, Seoul 04763, South Korea*

[4]*Department of Physics, Chungbuk National University, Cheongju 28644, South Korea*

[5]*Department of Physics, University of Maryland, College Park, MD 20742, USA*

[6]*Department of Electrical Engineering and Computer Science, University of Maryland, College Park, MD 20742, USA*

[7]*Quantum Technology Center, University of Maryland, College Park, Maryland, 20742, USA*

Contents

S1. Sensitivity of a N-*V* diamond magnetometer using lock-in detection

S2. Simulation of N-*V* fluorescence collection efficiency

S3. Characterization of N-*V* diamond samples using electron spin resonance (ESR) and Fourier transform infrared absorption (FTIR) spectroscopy

S4. ODMR spectra for all N-*V* orientations

S5. ODMR intensity vs. polarization angle

S6. Asymmetry in N-*V* resonance frequency shift with respect to magnetic field change

S7. Effect of dual frequency driving

S8. Temperature calibration measurement of diamond sample

S9. Simulation of N-*V* diamond sensor nonlinear response and sampling imperfections

S10. Configuration of bias magnetic field and test field

S1. Sensitivity of a N-*V* diamond magnetometer using lock-in detection

In a continuous-wave optically detected magnetic resonance (CW-ODMR) measurement, phase-sensitive lock-in detection with microwave frequency modulation records the derivative of an ODMR peak as depicted in Fig. S1(a). Given the linewidth Δf and contrast C, the slope α of the lock-in signal can be estimated as $\frac{CV_0}{\Delta f}$. When a time-dependent magnetic field $B(t)$ is applied along one of the N-*V* spin orientations, the output of the lock-in signal is $S(t) = sign * \alpha\gamma B(t)$, where γ is the N-*V* gyromagnetic ratio (2.8 MHz/G). The value of $sign$ can be ± 1, depending on the transition Δm_S (as described in the main text).

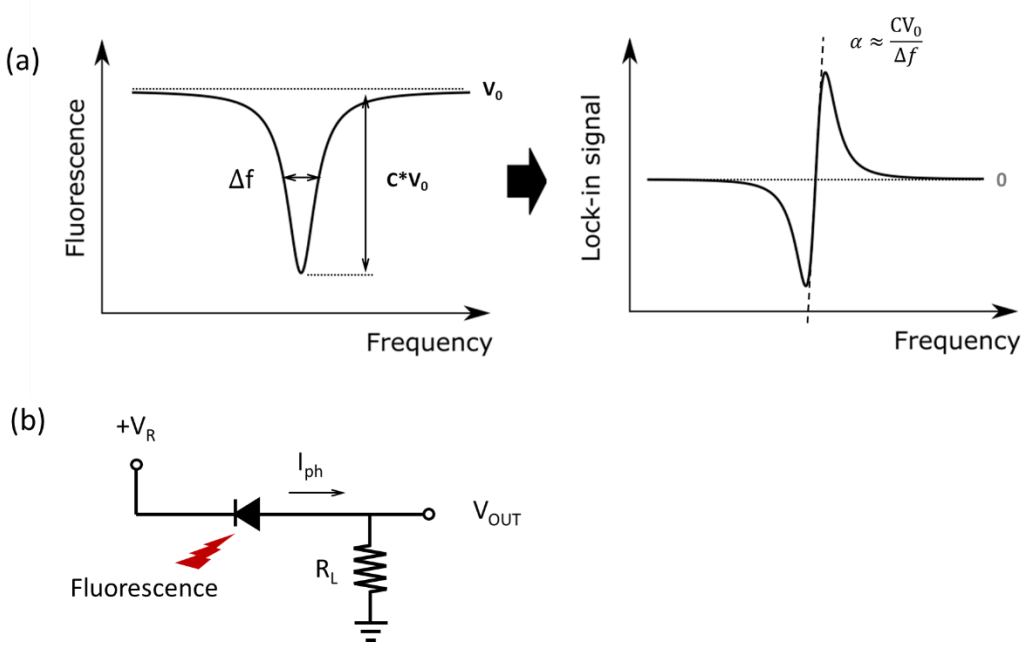


Figure S1. (a) Illustration of an ODMR peak and lock-in detection curve. (b) A simple model of optical detection of N-*V* fluorescence, including only photodiode and load resistance.

To obtain the equation of the shot-noise limited sensitivity of an N-*V* diamond magnetometer, we can represent the optical detection using the circuit diagram shown in Fig. S1(b). A photodiode produces a photo-induced current i_{ph} under a reverse voltage $+V_R$, when N-*V* fluorescence is incident on the detector. i_{ph} becomes the source of electric shot-noise current, and its noise spectral density (NSD) is $\sqrt{2ei_{ph}}$. The load resistance R_L transduces current into voltage. Thus, for the output voltage of the optical detection, $V_0 = R_L i_{ph}$ and NSD is $R_L\sqrt{2ei_{ph}}$. (Note that, if $i_{ph}R_L > 2kT/e$, Johnson noise of the load resistance can be ignored [S1]) Assuming that the lock-in amplifier imposes negligible noise on the output voltage of the optical detection, the magnetic field sensitivity η_B should satisfy the

shot-noise relation:

$$\alpha \cdot \beta \cdot \eta_B = R_L\sqrt{2ei_{ph}} \qquad \text{(S1)}$$

where β $(= \frac{df}{dB})$ is the derivative of the N-*V* resonance frequency with respect to magnetic field B, which is $\frac{\gamma}{2\pi}$ when B is aligned with the N-*V* symmetry axis. Using the expressions for α and β, η_B can be obtained as below,

$$\eta_B = \frac{\Delta f}{\frac{\gamma}{2\pi}C}\sqrt{\frac{2e}{i_{ph}}}. \qquad \text{(S2)}$$

S2. Simulation of N-*V* fluorescence collection efficiency

We calculated the collection efficiency of the fluorescence from N-*V* centers embedded in a diamond membrane by a FDTD simulation (Lumerical, Ansys Inc.). In our calculation, a 3-μm-thick diamond membrane is sandwiched by a quartz substrate and a half ball lens with refractive indices n_S=1.55 and n_L=2.0 (S-LAH79), respectively. The refractive index of diamond is 2.42. N-*V* centers are assumed to be distributed at the center of the diamond membrane. To obtain the average fluorescence collection efficiency from N-*V* centers with random orientation, we performed 2-dimensional calculations for three orthogonal dipole orientations (along *x*, *y*, and *z*), and averaged the collection efficiency. With the help of the elliptic reflector, the emission into -90° ≤ θ ≤ 90° is assumed to be detected. For n_L=2.0, the estimated collection efficiency is calculated to be 57.36 %, 50.81 %, and 61.20 % for a dipole oriented along *x*, *y*, and *z*-axes, which results in an average value of 56.45 %.

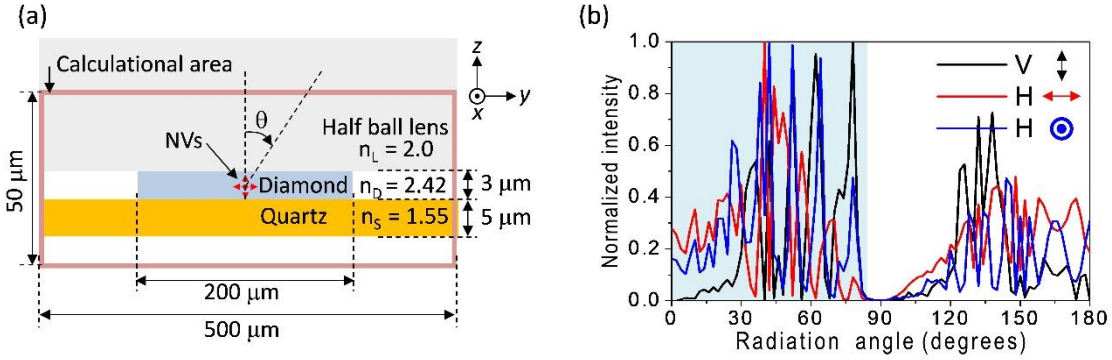


Figure S2. (a) Optical configuration used in the numerical simulation of N-*V* fluorescence collection efficiency. The red box represents the region considered in the calculation. (b) Normalized angular θ dependence of the radiation from a single N-*V* dipole. Complex patterns are obtained, which are summed for averaging. Backward fluorescence is also noticeable.

S3. Characterization of N-*V* diamond samples using electron spin resonance (ESR) and Fourier transform infrared absorption (FTIR) spectroscopy

Room temperature continuous wave ESR and infrared absorption measurements were made with a JEOL JES-X310 spectrometer at approximately 9.4 GHz and a Nicolet iN10MX FTIR spectrometer, respectively, to determine the negatively charged N-*V* center (NV^-) and substitutional nitrogen (N_s^0) concentrations in the diamond sample used in this work after electron irradiation and annealing . ESR spectral features around the NV^- transitions were fitted to Tsallis functions. The fit (red color) was integrated twice to obtain the area of ESR absorption spectrum for the estimation of the concentration [S2]; see Fig. S3(a).The initial N_s^0 concentration is about 30 ppm. Post-treatment, NV^- concentration was estimated to be about 0.5 ppm by comparing the integrated NV^- and N_s^0 signals to a reference sample with a known N_s^0 concentration of about 177 ppm, as determined from FTIR (Fig. S3(b)). Similarly, the concentration of N_s^0 was estimated to be about 1.3 ppm. The NV^- yield from annealing is approximately 1.7%; one of the reasons for the low yield may be the formation of di-nitrogen interstitial defects (H1a). The H1a defect arises from irradiating HPHT diamond by electrons or neutrons and has absorption feature in FTIR spectra at 1450 cm^{-1}, see Fig. S3(b) [S3].

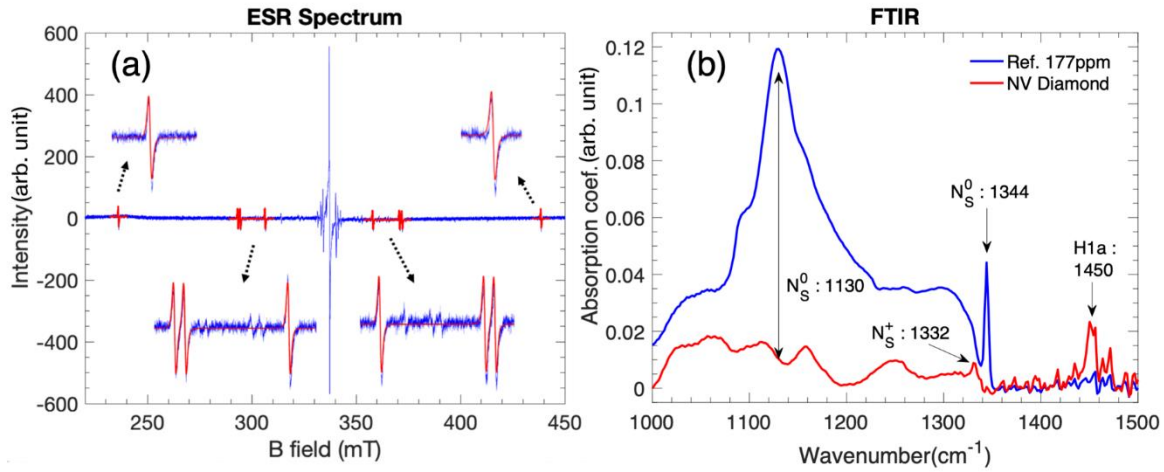


Figure S3. (a) ESR and (b) FTIR spectra of N-*V* diamond at room temperature. For the ESR spectrum, an external magnetic field was applied along the [111] axis of the N-*V* diamond. The blue and red lines in the ESR spectrum indicate the experimental data and the fit for NV^- transitions, respectively. Tsallis functions were used for the fit [S2] and the concentration of NV^- and N_s^0 were determined to be about 0.5 ppm and 1.3 ppm, respectively. The FTIR spectra of un-irradiated (blue) HPHT diamond and the N-*V* diamond (red) are shown in the right panel. We found various defects such as remaining nitrogen (N_S^0), positively charged nitrogen (N_s^+), and di-nitrogen interstitial (H1a). The low NV^- yield (≈1.7%) is attributed to the formation of H1a defects.

S4. ODMR spectra for all N-*V* orientations

An external magnetic field $\vec{B}$ was produced by a permanent magnet. The orientation and location of the magnetic field was controlled by a combination of manual rotation and translation stages. Figure S4 (a) shows the ODMR spectrum when $\vec{B}$ is aligned parallel to the [111] orientation of the N-*V* diamond sample. Blue dots are experimental measurements, while the blue line is a summation of the red, green, orange, purple lines, which correspond to numerical fits to the four NV orientation classes, NV1, NV2, NV3, NV4, as shown in Fig. S4(d), respectively. To confirm that the overlapped peaks indeed contain information from orientations NV2, NV3, and NV4, we repeated the measurements and fits with the angle of $\vec{B}$ purposely titled by 10 degrees (Fig. S4(b)) and 20 degrees (Fig. S4(c)).

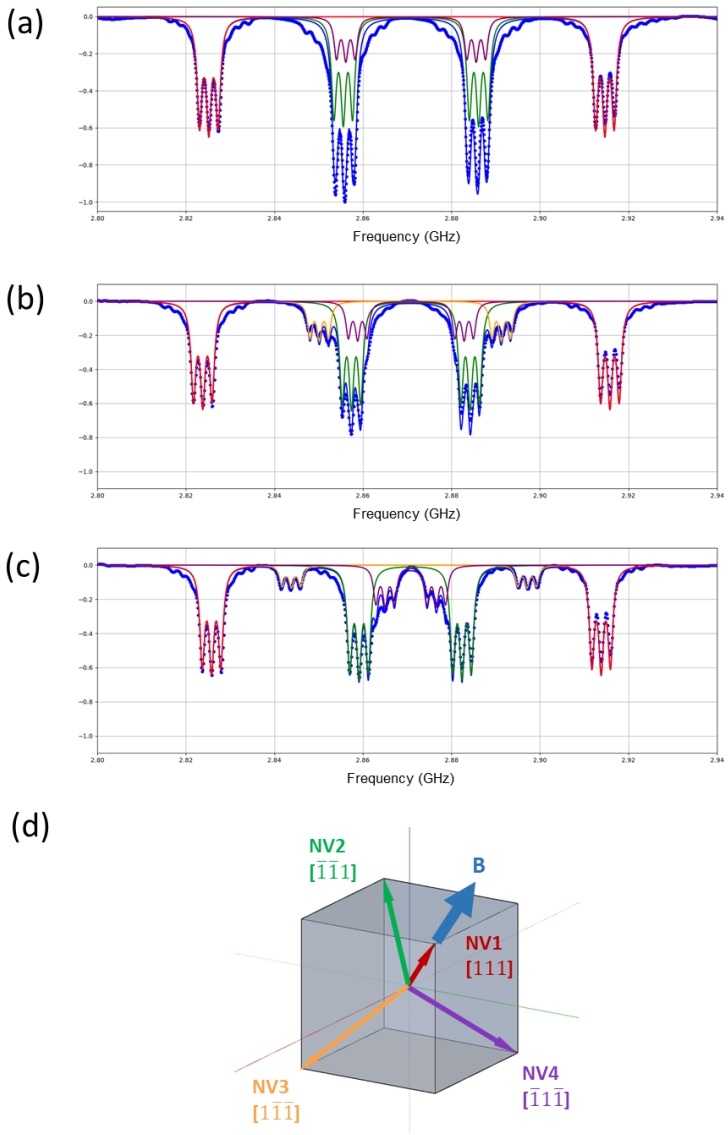


Figure S4. (a) Variation of ODMR spectrum when B is aligned along [111]; (b) tilted away from [111] by 10 deg.; (c) and by 20 deg. (d) The four orientations of N-*V* centers in diamond are distinguished by different colors.

S5. ODMR intensity vs. polarization angle

In Fig. S4(a), the observed intensity of the ODMR peak where NV2, NV3, and NV4 are overlapped is not three times as high as that from NV1. The polarization ($\vec{E}$) of the pumping laser must be taken into account to explain this effect. When an N-*V* center is orientated along the z axis, two optical transition dipoles $\overrightarrow{d_1}$ and $\overrightarrow{d_2}$ lie along the x and y axes, respectively. The N-*V* fluorescence intensity I is then proportional to $\left|\left(\overrightarrow{d_1}\cdot\vec{E}\right)^2+\left(\overrightarrow{d_2}\cdot\vec{E}\right)^2\right|$. With proper coordinate rotations, we calculated the variation of the ODMR peak intensity as a function of the polarization angle θ of ($\vec{E}$ (shown in Fig. S5(b)) for the four N-*V* orientations (Fig. S4(d)). Assuming the pumping laser is linearly polarized and incident orthogonally to the diamond sample, the polarization angle θ is defined with respect to the [100] N-*V* axis. The result shown in Fig. S5 (a) indicates that when $\vec{E}$ is orthogonal to a particular NV orientation, the intensity is maximum. For instance, when $\theta = 135°$, $\vec{E}$ is parallel to $[\bar{1}10]$. Then, NV1 and NV2 reveal the max intensity. Normalized by the max intensity, the intensity of NV3 and NV4 are 0.33 equally. This result explains the observed peak intensities of the spectrum in Fig. S4 (a). As stated in the main text, all the ODMR peaks from NV1, NV2, NV3, and NV4 will overlap when B is applied along the [001] orientation. Then, setting $\theta = 0°$ (or $90°$) will make the peak intensity maximum, 2.64 (4 * 0.66), as opposed to 4.

Note that the polarization angle does not actually increase the ODMR contrast (C) of a single N-*V* orientation, which is strongly governed by the intrinsic properties of the N-*V* center. However, when collecting the fluorescence from all four N-*V* orientations in an N-*V* ensemble, one finds that the effective contrast (C_i) of an ODMR peak intensity (I_i) from a single orientation class NV_i ($i = 1, 2, 3, 4$) increases with respect to the total intensity ($\sum_i I_i$). In Fig. S5 (a), we can see that the total intensity is constant (I_{tot}) irrespective of the polarization angle θ. Thus, C_i is a function of θ as below,

$$C_i = \frac{cI_i(\theta)}{\sum_i I_i} = c\frac{I_i(\theta)}{I_{tot}}. \qquad \text{(S3)}$$

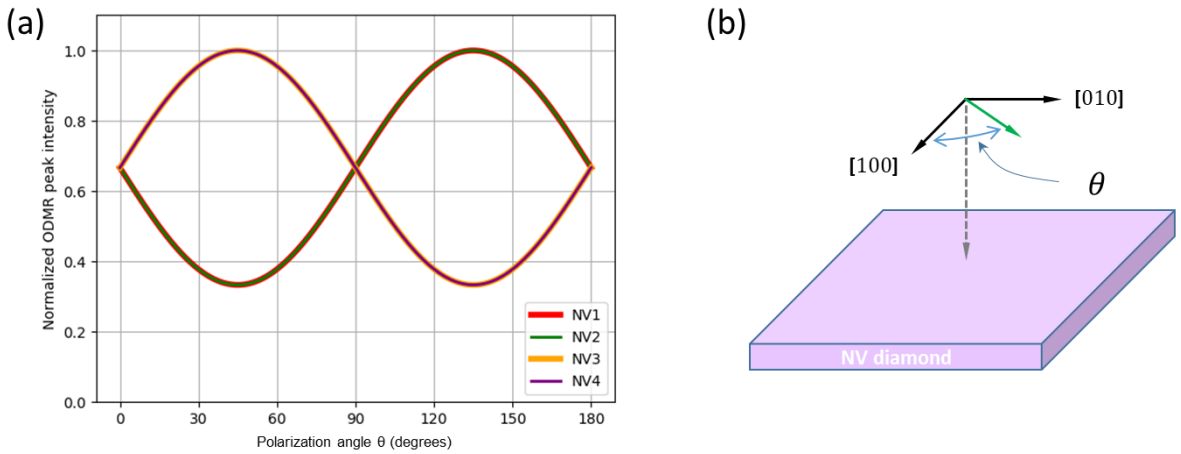


Figure S5. The variation of the ODMR peak intensity is calculated (a) as a function of the polarization angle θ of the pumping laser's optical electric field ($\vec{E}$ defined in (b) for the four N-*V* orientations (Fig. S4 (d)) and assuming the laser is incident orthogonally to the diamond sample.

S6. Asymmetry in N-*V* resonance frequency shift with respect to magnetic field change

Dual frequency driving employs both of the N-*V* spin resonances associated with $\Delta m_S = +1$ (HP) and $\Delta m_S = -1$ (LP). The lock-in slopes for HP and LP should be balanced to achieve a high isolation factor during multiplexed sensing of magnetic field and temperature. We observed asymmetry in the lock-in slopes of HP and LP as result of frequencies (f) associated with the LP and HP resonances having generally different sensitivities to magnetic field change ($\delta\vec{B}$), depending on details of the magnetic field alignment.

Figure S6 (a) shows calculations of the derivative of the N-*V* resonance frequency with respect to magnetic field for HP (thick line ▬) and LP (thin line —), as a function of magnetic field angle θ. To model the actual condition, the magnetic field was assumed to include a static term ($\vec{B}_0$) and a small varying term ($\delta\vec{B}$) as below,

$$\begin{aligned} \vec{B}_0 &= B_0[\cos(\theta_0)\,\hat{z} + \sin(\theta_0)\,\hat{k}] \\ \delta\vec{B} &= \delta B[\cos(\theta)\,\hat{z} + \sin(\theta)\,\hat{k}] \end{aligned} \quad \text{(S4)}$$

Here, the unit vectors $\hat{z}$ and $\hat{k}$ are parallel to [001] and [110], respectively. θ_0 = 54.7°, so $\vec{B}_0$ is along the [111] orientation with a magnitude of 1.6 mT (chosen to match the experimental results). The derivatives ($\beta = \frac{\delta f}{\delta B}$) are numerically obtained from the Hamiltonian of the N-*V* spin.

In Fig. S6, when θ is 54.7°, $\delta\vec{B}$ is parallel to NV1 or [111], which is indicated by the blue vertical lines.

Then, the derivative becomes the gyromagnetic ratio $\frac{\gamma}{2\pi}$ ($\pm$28 MHz/mT). NV1 reveals symmetrically inverted curves for HP and LP, because the static field $\vec{B}_0$ is parallel to NV1. However, for other field orientations, HP and LP are asymmetric because $\vec{B}_0$ is misaligned for those orientations. The lines for NV3 and NV4 are overlapped so not distinguishable. The lock-in slope is proportional to the contrast C and the derivative β, and directly indicates the field sensitivity. Figure S6 (b) depicts the calculated lock-in slopes; the lines for NV1 are colored red as before, but the blue lines include NV2, NV3, and NV4, since they are overlapped as shown in Fig. S4 (a) in the presence of $\vec{B}_0$. The dashed lines are the difference between the lock-in slopes of HP and LP, and summarize the results.

In summary, N-*V* spins aligned with static magnetic field provide a high isolation factor in multiplexed sensing. With other N-*V* spin orientations, balancing the sensitivities of HP and LP may not be feasible, particularly when a small magnetic field varies its orientation as well.

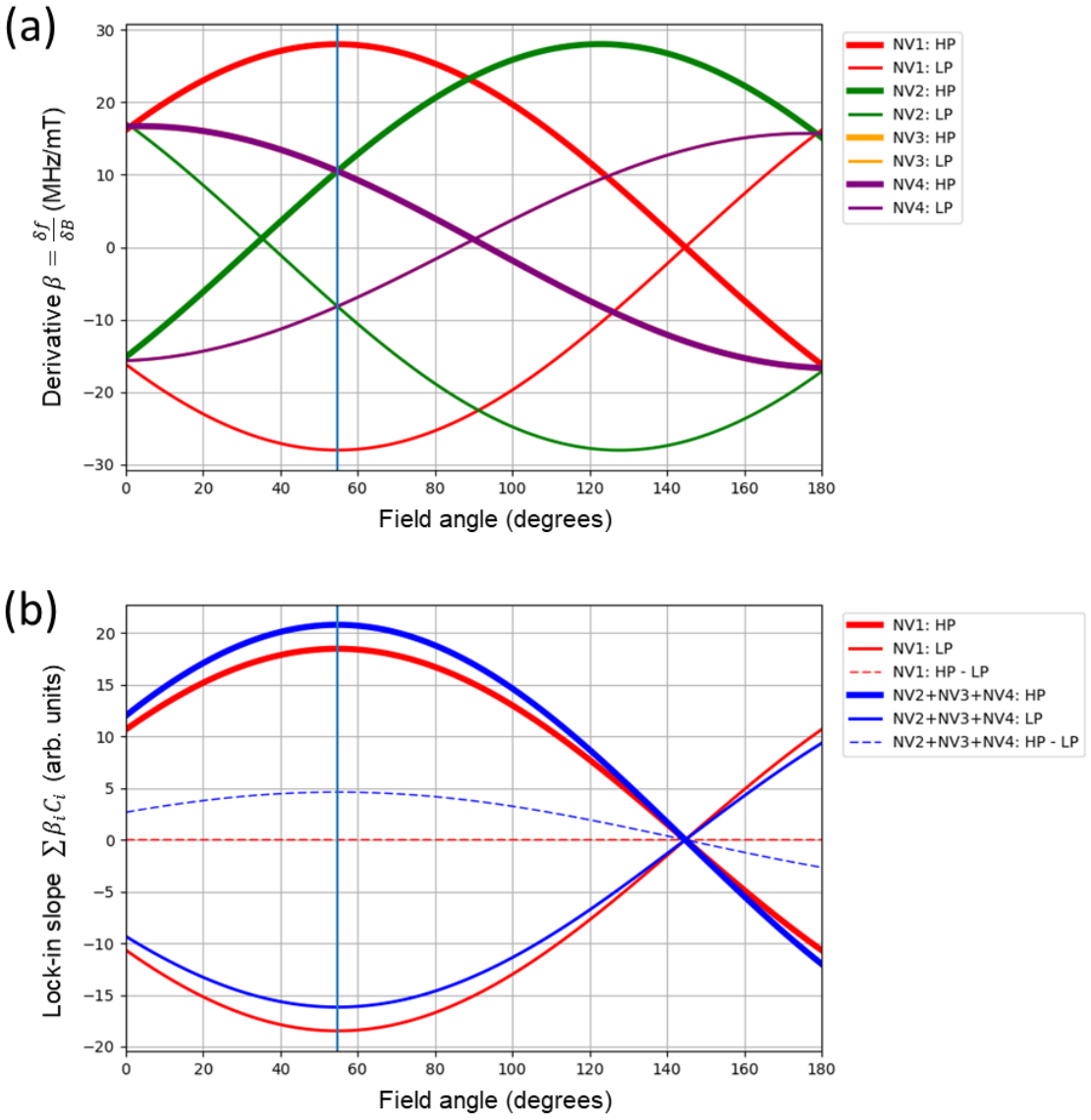


Figure S6. (a) The derivatives of N-*V* electronic spin resonance frequencies with respect to magnetic field are calculated as a function of the field angle. HP corresponds to $\Delta m_S = +1$, while LP to $\Delta m_S = -1$. (see Section S6 for details) (b) From the derivatives and contrasts, the lock-in slopes are obtained for NV1 (red) and the other orientations including NV2, NV3, and NV4. The dashed lines show the differences between HP and LP.

S7. Effect of dual frequency driving

To explicitly visualize the effect of dual frequency driving, we applied a test magnetic field at 10 Hz for 1 min. Figure S7 displays the observed signal when the N-*V* diamond sensor functions as a magnetometer ($f_1^R = f_2^R$ and $\phi_1^R - \phi_2^R = \pi$, described in the text), intended to record magnetic field only. Note that, in the middle of the test measurement for 30 s, one of the microwave sources was turned off. One can notice that with single frequency driving, the signal amplitude became about half of that with dual frequency driving. In addition, the baseline shows a noticeable drift, which typically

occurs without suppression of ambient temperature change. When the second microwave source is turned back on at approximately 45 seconds, the signal returns to the initial amplitude and baseline.

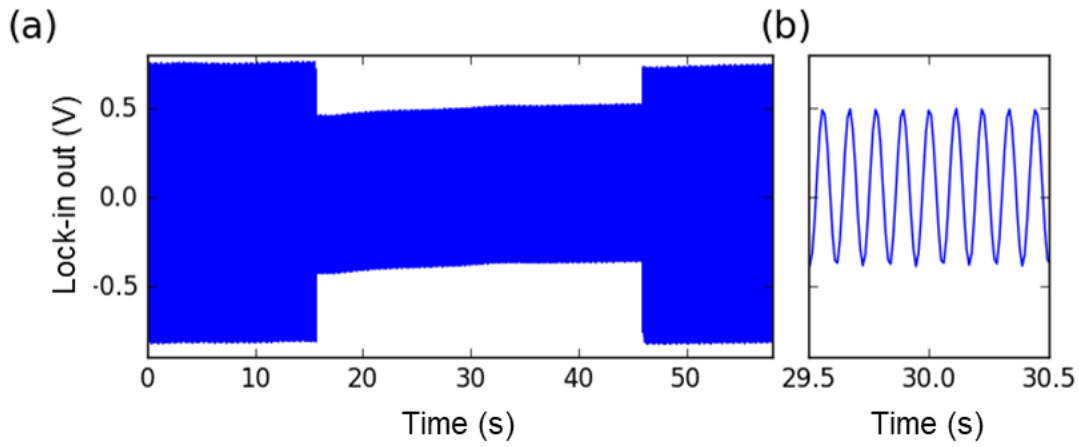


Figure S7. (a) Output signal of lock-in amplifier in the presence of a test magnetic field when the parameters for dual frequency driving are set for N-*V* magnetometer operation. In the middle of the test, one of the microwave sources is turned off. (b) Expanded view of signal for a duration of 1 s.

S8. Temperature calibration measurement of diamond sample

For calibration of the N-*V* diamond thermometer, we additionally mounted a non-magnetic temperature sensor (PT100) on the sapphire plate. As shown in Fig. S8, the temperature sensor is mounted on the same plane as the microwave antenna. The N-*V* diamond chip is positioned on the opposite side of the sapphire plate. The PT100 sensor was pre-calibrated (Lakeshore); and mounted in a copper block to shield electromagnetic fields. The distance from the center of the PT100 to the N-*V* diamond is less than 10 mm. A thermally conductive epoxy (Epoxy Tech., H20E) is used to glue the copper block on the sapphire plate, thereby providing a good thermal link between the PT100 sensor and the diamond sample.

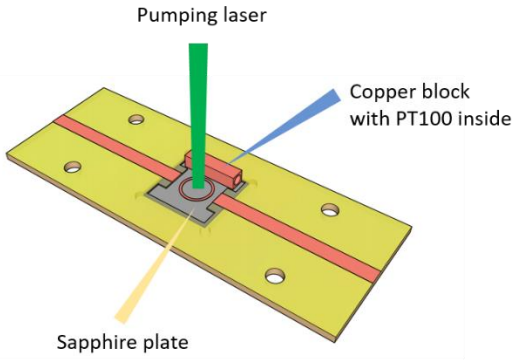


Figure S8. Set-up for calibration of the NV thermometer.

S9. Simulation of N-*V* diamond sensor nonlinear response and sampling imperfections

To investigate limitations of the isolation factor and potential sources for the observed higher harmonics in Fig. 4 of the main text, we performed simulations of the expected N-*V* diamond sensor signal as a function of applied magnetic field strength, errors in balancing of the two signals when operating in multiplexed mode, and which N-*V* resonances were probed. We simulate an ODMR signal in Fig. S9(a) through the summation of three Lorentzian curves separated by the N-*V* hyperfine coupling for both the lower and upper resonances. For the outer hyperfine resonances, the points of maximum and minimum slope, denoted by the orange and yellow dots, are not symmetric about the line-center due to the contribution of neighboring hyperfine peaks. This effect is increased with broadened resonances due to larger resonance overlap.

We fix the sensing conditions about the points of maximum slope and increase the amplitude of the applied magnetic fields. With increasingly large changes in the magnetic field and static sensing conditions, the nonlinear portion of the resonance is probed, leading to the increased presence of higher harmonics in the Fourier transform as shown in Fig. S9(b). With future measurements, we can mitigate these harmonics through fast feedback on the carrier frequencies to stay within the linear regime of the resonances.

In Figure S9(c), we intentionally modified the resonances to unbalance the slopes and cause asymmetries in the samplings of the lower and upper resonances. We find that this leads to the rise of even higher harmonics in the N-*V* magnetometry signal. Under realistic measurement conditions such asymmetries are expected due to drifts in ambient temperature, bias magnetic field orientation and magnitude, mw field amplitude, and optics.

Finally, we probe the role that sampling on the left-most resonance has on the rise of nonlinear phenomena compared to sampling on the middle resonances. We find in Fig. S9(d) that sampling on the middle hyperfine features of the lower and upper resonances would protect from nonlinearities at the applied field strengths; however, due to the coherent population trapping (CPT) effects explored in the main text, we were unable to sample these resonances. We note that this protection from nonlinearities is unstable and highly dependent on sampling symmetrically about the Lorentzian line center.

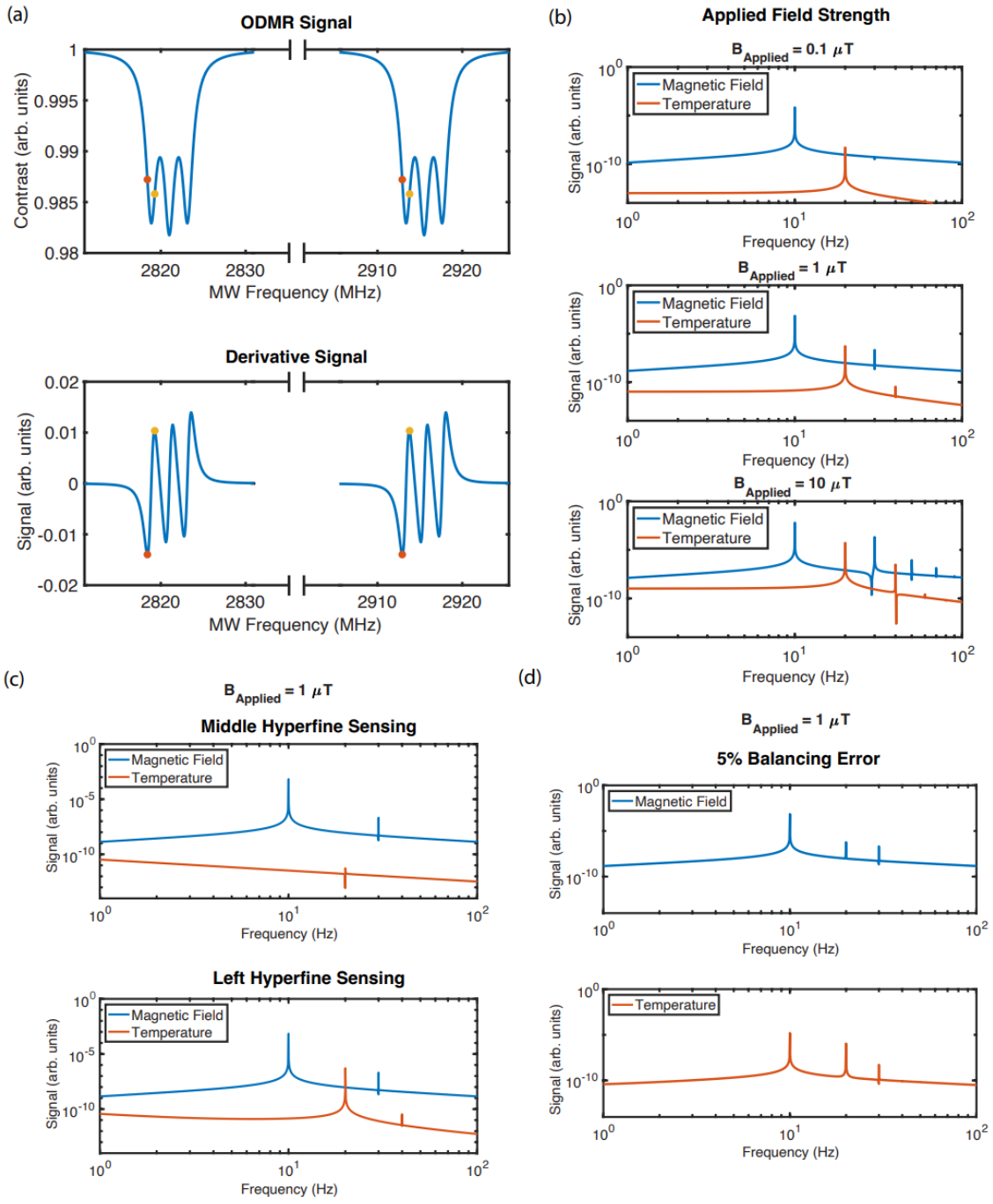


Figure S9. Nonlinear and sampling error simulations. (a) Simulated ODMR spectra for lower and upper resonances. (b) Increase in higher harmonics with strong applied magnetic fields in the simulation. (c) If the middle hyperfine resonances were used, then nonlinear effects would be further suppressed with a 1 μT magnetic field. (d) Simulation results when a 5% difference is added to lower and upper resonance slopes. The presence of even harmonics in the magnetic signal becomes apparent.

S10 . Configuration of bias magnetic field and test field

Figure S10 illustrates the orientations of the applied test magnetic field ($\overrightarrow{\Delta B}$) at 10 Hz. and the static bias field ($\overrightarrow{B_0}$). $\overrightarrow{\Delta B}$ is applied along the [100] orientation, normal to the surface of N-*V* diamond, with a magnitude of about 1.73 μT (RMS). Thus, the projected magnetic field along the [111] N-*V* orientation is $\Delta B_z \approx 1$ μT as shown in Fig. S10(a). A bias field of 1.6 mT is nearly aligned to the [111] orientation. So, θ_t in Fig. S10 is nominally 54.7°. However, as calculated in the main text, the experimentally-obtained isolation factor implies a residual misalignment angle θ_B of 0.3°.

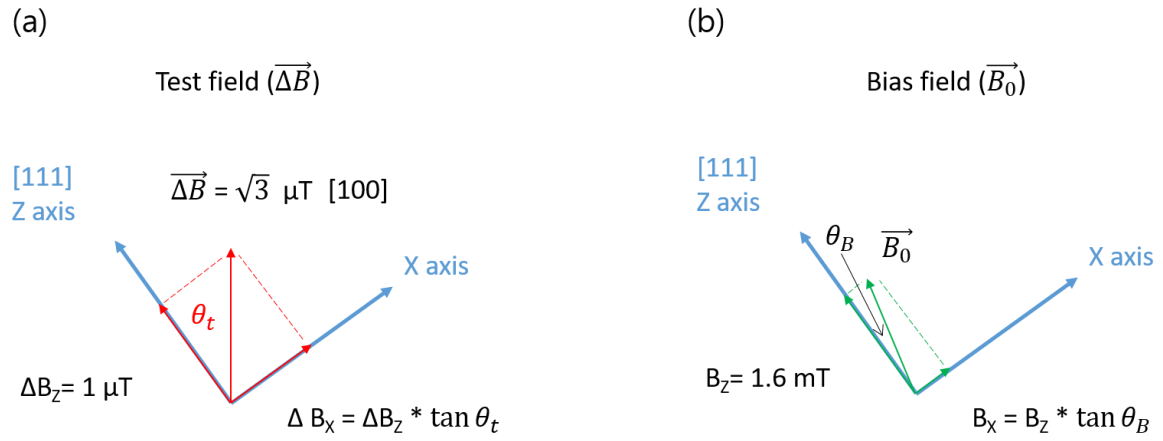


Figure S10. Experimental configuration of test magnetic field and bias magnetic field with respect to the [111] orientation of N-*V* diamond.

References

S1. Philip C. D. Hobbs, *Building electro-optical systems*, John Wiley & Sons, inc., Hoboken, New Jersey (2009).

S2. D. F. Howarth, J. A. Weil, and Zbigniew Zimpel, Generalization of the lineshape useful in magnetic resonance spectroscopy, J. Magn. Reson. **161**, 215 (2003).

S3. V. M. Acosta, E. Bauch, M. P Ledbetter, C. Santori, K. -M. C. Fu, P. E. Barclay, R. G. Beausoleil, H. Linget, J. F. Roch, F. Treussart, S. Chemerisov, W. Gawlik, and D. Budker, Diamonds with a high density of nitrogen-vacancy centers for magnetometry applications, Phys. Rev. B **80**, 115202 (2009).